Lyle, M., Koizumi, I., Richter, C., and Moore, T.C., Jr. (Eds.), 2000
Proceedings of the Ocean Drilling Program, Scientific Results, Vol. 167

29. *DATA REPORT:* COLOR RECORDS FROM THE CALIFORNIA MARGIN: PROXY INDICATORS FOR SEDIMENT COMPOSITION AND CLIMATIC CHANGE[1]

Alexandra J. Nederbragt,[2] Jürgen W. Thurow,[2] and Russell B. Merrill[3,4]

INTRODUCTION

The growing importance of high-resolution paleoceanographic studies in recent years has increased the need for methods that allow fast and easy compilation of long, detailed, and continuous time series. Sediment color is one property of the sediment that reflects chemical composition and, to some extent, physical properties, and as such can be used as a proxy for paleoceanographic studies. Composition of the sediment flux, and its preservation at the sediment/water interface, is controlled by climatic factors (e.g., weather, current patterns, surface water productivity, and water column stratification). Thus color variations offer a proxy to variations in the external factors that control sedimentation and thus a monitor of regional and (or) global climate change. Deep-sea sediments are particularly suitable for such an approach because their composition is relatively simple. This allows color changes to be correlated directly with variations in one or at most a few sediment components, when color measurements are calibrated against discrete geochemical and sedimentological analyses.

Quantitative color measurements are now routinely produced during cruises of the Ocean Drilling Program (ODP), to generate color time series that provide a means for correlating parallel holes. The Oregon State University spectral reflectometer (Mix et al., 1995) or the Minolta spectrophotometer allow the collection of discrete measurements that form an average over some surface area of sediment. In contrast, a much higher stratigraphic resolution can be obtained from digital images of the core surface, as each pixel in the image represents one measurement. The actual resolution depends on the camera and its distance from the sediment, but an effective resolution of one measurement per 100 µm, or better, can easily be obtained with modern cameras and computers. To test different color-data collection systems for suitability for use on board, a video-camera system was used during ODP Leg 167 for continuous imaging of all cores that were drilled (Lyle, Koizumi, Richter, et al., 1997). The ultra-high resolution time series that can be obtained from such images have been used to unravel the climatic history on annual to centennial scales represented in annually laminated sediments (Merrill and Beck, 1995; Schaaf and Thurow, 1995, 1998).

The video system used during Leg 167 is essentially the same as that described by Merrill and Beck (1995), who tested the system and developed software for image capture and processing. The system was brought aboard for further testing, to determine whether it warranted inclusion in the standard shipboard analytical tools. Video images of discrete, overlapping segments of sediment potentially offer a method for archiving of sedimentary structures, but in addition, high-resolution time series of color variation can be derived from these images. Automated processing and mosaicing of individual images containing a 20-cm segment of sediment allowed the compilation of a color time series while keeping up with the core flow (Lyle, Koizumi, Richter, et al., 1997). However, it was found that the procedures used to convert video color to continuous time series were not able to deal adequately with several practical problems that arose during the leg, the main two being:

1. The standard method (Rogers, 1985) that was used to convert the red, blue, and green (RGB) in the video images to color-coordinates more suitable for presentation (L*a*b* system defined by the Commission Internationale de l'Éclairage [CIE]) was found not to be adequate. Recalibration of the camera during the drilling of Site 1019 produced a change in calculated color output, resulting in an offset in values for sections drilled before and after the recalibration (Fig. 1).
2. Correction for nonuniform distribution of the illuminant was based on the pattern observed in images of a neutral gray card that was scanned regularly during the cruise. However, distribution of especially L* (lightness of the sediment) within an image is highly dependent on the reflectivity of a surface, and correction curves calculated from the gray card were too flat to handle the more steeply curved color data produced by wet (more reflective) sediment surfaces (Fig. 2).

It was therefore desirable to reprocess the images to obtain better calibrated color time series. Here we describe modified methods for processing the image data and present the updated color records.

METHODS

Imaging

The imaging system that was used during Leg 167 consisted of a SONY DXC-750MD NTSC camera with three charge-coupled device (CCD) arrays of 768 × 493 cells and a Fujinon TV.Z 4 × 7.5 lens. The camera registers the three channels, red (centered at 700 nm), green (546 nm), and blue (436 nm), simultaneously, which reduces the possibility that shipboard vibration will affect the quality of the image. For lighting, two 200-watt, daylight-balanced Hydrargyrum Medium Arc Iodide (HMI) lamps were used, which have an initial color temperature of 5600°K. The manufacturer stated that the color temperature of the lamps would decrease at a rate of 1°K/hr. In practice, however, the color temperature trend turned out to be less predictable.

Cores were imaged in steps of 20 cm, with each image originally having an overlap with surrounding images, covering around 25 cm of sediment in a 24-bit image of 1008 pixels along the core axis by 486 pixels across the width of the core. To reduce storage requirements as much as possible, all images were trimmed automatically, reducing the overlap to 0.3 cm. The effective resolution along the stratigraphic axis translates into ~40 measurements (pixels) per centimeter of sediment (0.25 mm).

With each segment of sediment, a ruler was photographed with a black and white bar code that would allow automated recognition of the exact interval within a 1.5-m section. Each image also contains a

[1]Lyle, M., Koizumi, I., Richter, C., and Moore, T.C., Jr. (Eds.), 2000. *Proc. ODP, Sci. Results,* 167: College Station TX (Ocean Drilling Program).
[2]Department of Geological Sciences, University College London, Gower Street, London WC1E 6BT, United Kingdom. Correspondence author: j.thurow@ucl.ac.uk
[3]Ocean Drilling Program, Texas A&M University, 1000 Discovery Drive, College Station TX 77845-9547, USA.
[4]Present address: Queens College, City University of New York, 65-30 Kissena Boulevard, Flushing NY 11367, USA.

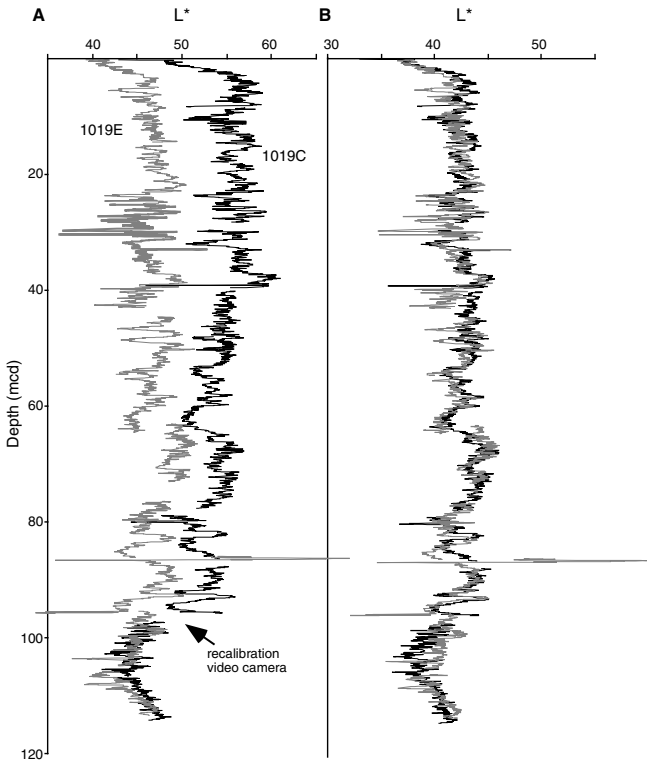

Figure 1. Site 1019 L* record comparing results of standard RGB to L*a*b* conversion (**A**) with those of the four-color conversion developed in this study (**B**). Black line = Hole 1019C, gray line = Hole 1019E. The standard conversion cannot compensate for a recalibration of the video camera during the scanning of Hole 1019C. The nearly identical values produced by the four-color approach show that camera effects are successfully filtered out. For further discussion, see text.

color reference card with red, green, blue, gray and white chips, for which the color values in the XYZ tristimulus color space have been determined for ODP. These reference chips are used for calibration of absolute color values of the sediments.

Data Processing

Time series are extracted from the images by extracting RGB values along a line through the image, converting the values to CIE L*a*b*, correcting each interval for inhomogeneities in the light distribution of the bulbs, and stacking all segments to a continuous time series. This process was fully automated during the cruise, to produce a preliminary time series while keeping up with the core flow. The reprocessing of the images that will be described here is only semiautomated. The various steps in the processing are done on all images in one run, but after each step, results are written to disk and checked for consistency. For each step, several relevant variables that summarize the results were plotted to be able to detect outliers that were due to incorrect handling of the data in a specific image. For example, correct recognition of the bar code, used to produce a depth scale, can be checked by plotting the calculated resolution for all images, as errors will result in aberrant values in pixels per centimeter of sediment. The actual order in which the various processing steps are done (e.g., color calibration, correction for inhomogeneous light distribution of the illuminant, filtering out of cracks and voids) is in itself not crucial; the order used here is mainly chosen for convenience.

In each image, a line scan of one pixel wide was collected at a fixed position in the image, which corresponds to approximately the center of the core surface. With the line scan, a line of pixels was collected from within the bar code, and the average RGB values were calculated for a 40 by 20 pixels large area from each of the red, green, blue, and gray chips on the color card. With these raw data as the basic input, the following steps were done to obtain the final filtered color time series.

RGB to L*a*b* Conversion

As a first step in the processing, measured RGB values in the line scan are converted to CIE L*a*b*. L* describes lightness; its values can range between 0 (black) to 100 (white). The other two variables describe the actual color, with a* representing green (negative values) or red (positive) and b* representing blue (negative) or yellow (positive values). CIE L*a*b* has as an advantage over other color systems because the three variables are the most easy to interpret in color as registered by the human observer. Translation into the L*a*b* system is done via an intermediate step, by translating RGB values into CIE XYZ (tristimulus) values. This intermediate step is crucial in obtaining calibrated color results that are reproducible independent of which camera system, light source, or calibration setting is used. The standard conversion from RGB to XYZ values, which was used shipboard, uses the following equation (Rogers, 1985):

$$\begin{bmatrix} X \\ Y \\ Z \end{bmatrix} = \begin{bmatrix} (X_R \cdot C_R) & (X_G \cdot C_G) & (X_B \cdot C_B) \\ (Y_R \cdot C_R) & (Y_G \cdot C_G) & (Y_B \cdot C_B) \\ (Z_R \cdot C_R) & (Z_G \cdot C_G) & (Z_B \cdot C_B) \end{bmatrix} \cdot \begin{bmatrix} R \\ G \\ B \end{bmatrix}, \quad (1)$$

where

X, Y, Z are the CIE tristimulus values of a color;

R, G, B are the red, green, and blue channels of a color as measured in the image;

X_R, Y_R, Z_R, and so on are the (unknown) chromacities of the RGB primaries of the camera; and

$$C = \frac{\text{tristimulus value of unit amount of camera primary}}{\text{chromacity of that primary}} \text{ for R, G, and B.}$$

However, for computational purposes, the terms $(X_R \cdot C_R)$, $(Y_R \cdot C_R)$, $(Z_R \cdot C_R)$, and so on are taken together as a single unknown constant each, giving

$$\begin{bmatrix} X \\ Y \\ Z \end{bmatrix} = \begin{bmatrix} X'_R & X'_G & X'_B \\ Y'_R & Y'_G & Y'_B \\ Z'_R & Z'_G & Z'_B \end{bmatrix} \cdot \begin{bmatrix} R \\ G \\ B \end{bmatrix}. \quad (2)$$

Equation 2 can be solved by inserting measured RGB values and known XYZ values for each of the red, green, and blue chips that were photographed with each segment of core. Writing out the three matrix multiplications and rearranging the equations yields three sets of three linear equations with three variables each.

This standard conversion implies that the lines calculated for X, Y, and Z intersect the origin of the axes (i.e., that pure black has values equal to, or very close to (0,0,0) in both the XYZ and RGB vector space). In practice, Equation 2 could not adequately estimate color values to give the same absolute values before and after a recalibration of the camera, which was done to correct for drift in the green channel. Therefore, Equation 2 was modified to allow for the presence of an offset from the origin, to take into account that the actual values produced by the camera for black and white are dependent on the setting

$$\begin{bmatrix} X \\ Y \\ Z \end{bmatrix} = \begin{bmatrix} a_1 \\ a_2 \\ a_3 \end{bmatrix} + \begin{bmatrix} X'_R & X'_G & X'_B \\ Y'_R & Y'_G & Y'_B \\ Z'_R & Z'_G & Z'_B \end{bmatrix} \cdot \begin{bmatrix} R \\ G \\ B \end{bmatrix}. \quad (3)$$

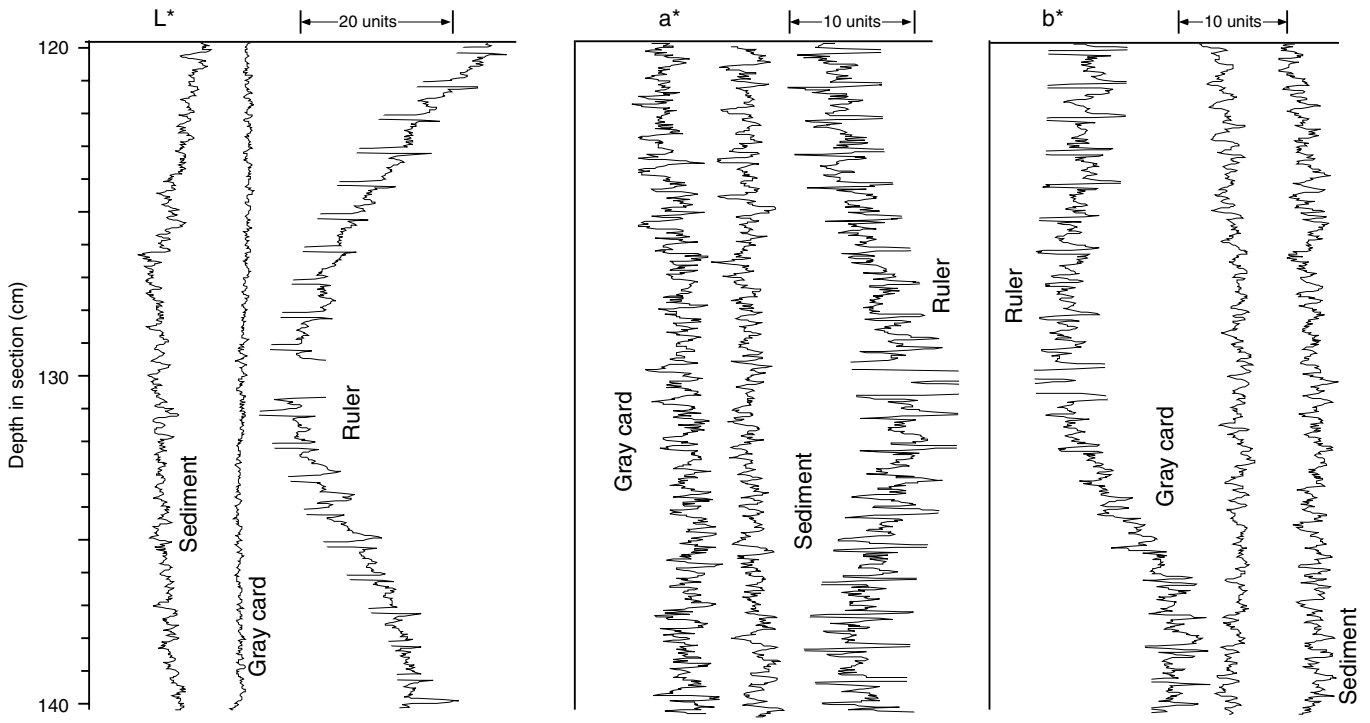

Figure 2. Examples of raw line-scan data through sediment and ruler in an image from Section 167-1019C-1H-1 and through a dull gray card, to illustrate how reflectivity of a surface influences the color distribution across the image. Curves are at the same scale in each variable but have been offset from the actual values for ease of interpretation.

In this case, information about four colors is needed to solve the constants (i.e. the red, green, blue, and gray chips). Writing out the matrix multiplication and rearranging the sets of linear equations yields the following for the X-values of the four color chips used:

$$\begin{bmatrix} X_r \\ X_g \\ X_b \\ X_{gr} \end{bmatrix} = \begin{bmatrix} 1 & R_r & G_r & B_r \\ 1 & R_g & G_g & B_g \\ 1 & R_b & G_b & B_b \\ 1 & R_{gr} & G_{gr} & B_{gr} \end{bmatrix} \cdot \begin{bmatrix} a_1 \\ X_R \\ X_G \\ X_B \end{bmatrix}. \quad (4)$$

Here, Rr, Gr, and Br, and X_r, Y_r, and Z_r are the measured video camera channels and the known XYZ values respectively for the red chip; subscripts g = green, b = blue, and gr = gray apply to the other three color chips used. This set of four linear equations with the four required constants as variables can be solved with standard methods; Y′ and Z′ constants are solved in an equivalent manner.

Equation 4 and its equivalents for Y′ and Z′ are solved for each image individually. Results show that the introduction of a vector of constants produces a better approximation of absolute color values than the standard three by three matrix conversion. Typically, values for the constants a_1, a_2, and a_3 are found to range between 1.5 and 4.5, demonstrating that an offset from the origin of the X, Y, and Z axes is indeed present. The result of the four-variable approach, after further conversion to L*a*b* values, produces similar values for parallel holes imaged before and after recalibration of the video camera (Fig. 1B). The four-variable matrix solution uses all the color information in the reference color card that was scanned with each image for this study (the white chip in the card is usually out of gamut). However, a reference card with more than four color chips would allow the constants to be solved for various combinations of four colors, thereby allowing statistical averages to be estimated.

The XYZ values estimated for the data in the line scan are then further converted to CIE L*a*b* values using the following equations (from Billmeyer and Saltzman, [1981]):

$$L^* = 116\left[f\left(\frac{Y}{Y_n}\right) - \frac{16}{116}\right], \quad (5)$$

$$a^* = 500\left[f\left(\frac{X}{X_n}\right) - f\left(\frac{Y}{Y_n}\right)\right], \quad (6)$$

$$b^* = 200\left[f\left(\frac{Y}{Y_n}\right) - f\left(\frac{Z}{Z_n}\right)\right], \quad (7)$$

with $f(Y/Y_n) = (Y/Y_n)1/3$ for $Y/Y_n > 0.008856$ and $f(Y/Y_n) = 7.787(Y/Y_n) + 16/116$ for $Y/Y_n \le 0.008856$; $f(X/X_n)$ and $f(Z/Z_n)$ are defined similarly. X_n, Y_n, and Z_n are the tristimulus values of a reference white. For this study, the known XYZ values of the white color chip are used as reference values.

Voids and Cracks

The conversion to L*a*b* is done as the first step, to facilitate detection of voids and cracks in the sediments, which in this color system can be easily recognized in the single variable L*, whereas all three variables are needed in other systems. Cracks in the sediments result in pixels that are darker than the surrounding sediment (have lower L* values) or, if voids are filled with foam, as much lighter pixels. Considering all values in one segment as a statistical distribution (or histogram), such voids and cracks should show up as outliers. For this study, extremes on either side of the distribution were removed, using as truncation limits (determined by trial and error) the first one-unit wide frequency class on either side with more then 10 measurements. The resulting truncation was checked by plotting the resulting maximum and minimum L* values for consecutive images. Segments with aberrant values were then inspected manually and adjusted if required. All values that were finally identified as outliers were then set to missing data. This includes voids and cracks, as well scratches in the core surface that produced dark shadows or very strong reflections. To compile an optimal time series, gas voids, which artificially add to the thickness, should actually be

subtracted from the composite depth scale. However, the present color data set retains the curated composite depth scale, to allow correlation with other data.

Light Correction

The images have to be corrected for the effect of a nonuniform distribution of the light source. The actual light distribution produced by the lamps across the imaged area can be estimated by measuring the departure from average in an image of a uniform gray card. However, this estimated light distribution, which was used shipboard to correct for light effects, is in practice not suitable to remove all artifacts from the sediment color time series. The actual departure from a flat line across an image depends largely on how reflective the imaged material is. The effective light distribution in sediment, which is wet, especially in the top cores, is more steeply curved than the distribution across the dull gray cards that were scanned for reference. The ruler in the image has a light curve that is again more steeply curved than the sediment (Fig. 2). The video system on board was not polarized. However, reflections produced by wet sediment can be reduced by polarization, but cannot be suppressed completely. For example, the shore-based ODP Leaf-digital imaging system, which is polarized, still produces sediment light curves that are steeper than those across a dull surface.

The result is that light correction can only use the sediment itself to estimate the departure from a flat line across an image that a homogeneously colored surface gives. As wetness of the sediment, and thus reflectivity, will vary from section to section, a light correction curve should be estimated for each image individually. One method would be to use the overlap between adjoining images. Although the steepness of the measured light curve varies, the basic shape remains constant. Using an overlap of several centimeters, the correction could be done by flattening the measured curves progressively until the best fit between pairs of overlapping images is obtained. This approach could not be tested as a method because the present data set does not have enough overlap between images to produce reliable results.

Light correction here was finally done by fitting polynomial least-square regression lines to each of L*, a*, and b* in each image, using pixel position within the line scan as the independent variable in the regression. However, the best-fit curve in a given individual segment will incorporate real variation in sediment color as well as the effects of the nonuniform distribution of the light source. By taking the average curve for a large set of images any systematic variation in real color at a decimeter scale, which will affect curves in individual images, is filtered out as it does not occur systematically in the same position in all images. In this case, we estimated one average light correction curve for each site separately. The departure from the mean of the values in the correction curve was then subtracted from the values in each line scan to correct for light distribution. The approach used here, while reducing the effects of the light source, cannot completely remove all artifacts, however, because a single average curve cannot account for steeper or flatter distributions in individual images. Indeed, some 20-cm cyclicity remains present in all sections as an artifact of light distribution, but in most sites the amplitude is much lower than that of the real color variation. However, for Site 1019, which has sediments that show only subtle variation in color, using the average regression curve for all images produced results in which a considerable amount of the total variation in color could be attributed to light distribution artifacts. Therefore, for Site 1019, several regression curves were calculated (i.e., for the top two cores in all holes together, and than for all remaining cores in each hole separately).

Further Filtering and Compilation

Further distortion in the color-data color is produced by the end-of-section markers, which were included as an aid in the automated processing. The markers, which lie on top of the split core liner, consist of white foam, edged with red (or blue) tape. Apparently, light reflects from this tape onto the sediment in the immediately adjoining part of the core surface. At least in practice, the 10 cm or so of sediment close to the end-of-section marker is found to give values in all three color variables that are consistently different from values in the rest of the section. The offset is only a few units, but it is large enough to be noticeable unless the real color variation has a high amplitude. To avoid potential artifacts, the deepest 10 cm in all sections was deleted from the final data set presented here.

The high resolution of 40 measurements per centimeter that is obtained from the images after the processing described above is not required to describe the usually decimeter- to meter-scale variation that is present in the Leg 167 sites. Therefore, data were reduced to smaller and more manageable data sets by taking the median value in each centimeter of sediment. Using the median rather than the mean allows further filtering of any outliers still present in the data set. All individual line scans per core were mosaiced into a continuous series, which was converted to a composite depth scale using the composite depth tables presented in Lyle, Koizumi, Richter, et al. (1997). Voids and cracks, which were removed from the data set, are still present as missing intervals in the final compilation, to ensure that all measurements are at the same depth scale as other analytical data.

COLOR DATA

Analytical Error

The way the images were collected was not designed to provide an estimate for analytical precision of the digital-image–based color measurement method. Even if a digital camera remains stable over a longer period of time, reproducibility of RGB values of a specific object is not in itself a measure for precision. The accuracy and precision of the final color data is mostly dependent on the processing steps (i.e., conversion to calibrated color values and correction for uneven light distribution within single images). We cannot as yet estimate the error involved in the data processing, but inspection of the generated color time series yields some rough measure of what the analytical accuracy of the method can be.

The fact that processed color values for Holes 1019C and 1019E are very similar, even though the calibration settings of the camera were changed considerably, shows that the imaging method can yield accurate color data (Fig. 1). The color-conversion equation developed here provides a method that is robust as far as changing the setting of a given camera is concerned. Further testing should show if consistent results can be obtained also when different camera systems and (or) different light sources are used to image one and the same object.

Visual examination of a* values, which, of the three color variables, has the lowest amplitude signal, shows that the noise level is low enough to recognize even subtle color trends. Figure 3 shows examples of parallel holes in two sites. Site 1010 has a low-amplitude signal in a* but shows a consistent trend in all three holes, which presumably registers a Milankovitch signal. Site 1022 shows a much weaker and less regular signal, which is less easily correlated between parallel holes. Presumably, a large part of the variation at that site is due to noise and may provide a first estimate of analytical precision. Wavelengths of 1 m and more were filtered out of the data in this interval at Site 1022, and the standard deviation was calculated over the remaining high-frequency data. Standard deviations are between 0.5 and 0.8 for all three color variables, depending on which hole is used. This provides a rough maximum estimate for the analytical error, which is sure to be an overestimation of the real error, as it includes “random” but real color variation as well as error attributable to the method. The main source of analytical error at present is in the way the correction for light is carried out. Here, an average regression curve for a large number of images is used to estimate a light correction curve, which means that individual images with flatter or

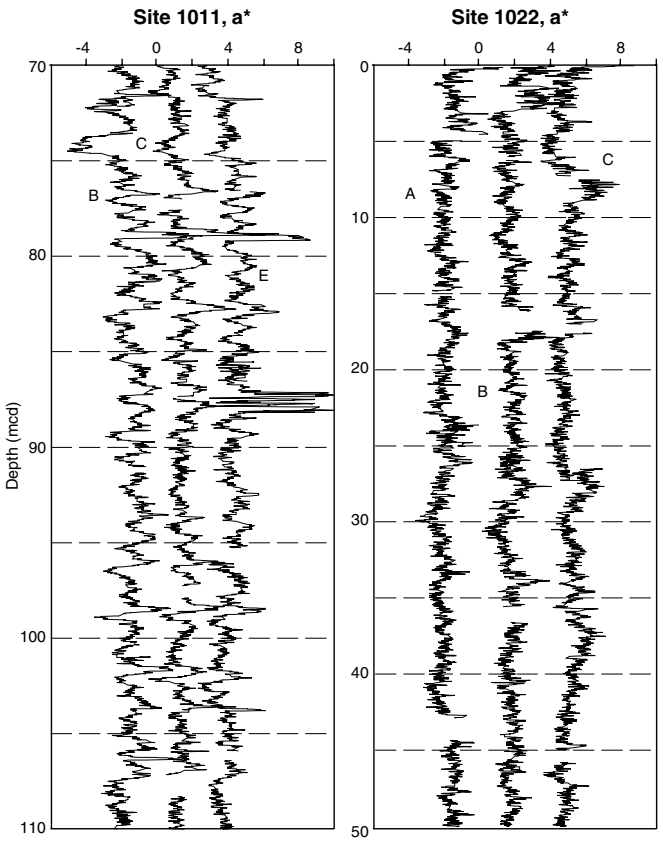

Figure 3. Examples of a* records in two intervals to illustrate visually that analytical precision is good enough to register even a low-amplitude signal consistently. Data for Holes 1011B and 1022A are at their original a* scale; the other holes (Holes 1011C, 1011E, 1022B, and 1022C) have been offset by three units. Note that the horizontal scale is the same in both plots.

steeper light deviations are not corrected adequately. On the other hand, given that real variation in color is present at decimeter to meter scale, using only a few images to estimate a correction curve could too easily result in a correction that filters out part of the real color variation. For now, the data contain a systematic error, which cannot be filtered out, with a deviation from the real color as a function of the position in the image relative to the light source. Future work will be done to test how an overlap of several centimeters between images can be used to refine the light-correction procedures, and thereby reduce the analytical error.

Color Time Series

The reprocessed digital image color data set included on the volume CD-ROM (back pocket, this volume) covers all sites drilled during Leg 167, except Site 1015. Part of the images for Site 1015 could not be retrieved from their storage medium for reprocessing, and, in combination with relatively low core recovery, the resulting time series is too incomplete to warrant inclusion. For all other sections, except Site 1022, composite depth was converted into an age scale by linear interpolation between shipboard age data. A zero age is assumed for the top of each site; ages for sediments below the oldest age-control point were assigned an age by extrapolating accumulation rates. Site 1022 has too few age control points to provide a meaningful age interpolation. Figures 4 through 6 present filtered composite records plotted against age, consisting of the shipboard splice, below which data from the deepest hole at each site are added.

A preliminary indication of how sediment composition determines color can be obtained from a comparison of color data with shipboard chemical data. Organic carbon (TOC) and carbonate content measurements and the semiquantitative estimates from smear slides are matched to color data points in the nearest centimeter in the section, and correlation coefficients are calculated between the compositional data and the three color variables (Table 1). For smear-slide data, only data from major lithologies were used; the sum of all siliceous microfossils is used as an estimate of biogenic silica (BSi) content. Clay content is included as a test for consistency of the semiquantitative data. Smear-slide and chemical samples cannot be matched directly, because they are not taken in the same interval; however, positive correlations between L* and carbonate and negative ones between clay and L* (Table 1) are as expected and suggest that smear-slide data are internally consistent. As such, BSi estimates can provide a useful first comparison with color data.

Figure 4 shows the color record for the three deep-water sites, Sites 1010, 1016, and 1021. At these sites, long-term variation at Ma-scale occurs in carbonate content (Lyle, Koizumi, Richter, et al., 1997). TOC is generally low. BSi is high in sediments older than 7 Ma in Sites 1010 and 1021 and is variable but high on average throughout the section at Site 1016.

L* correlates strongly with carbonate content; b* follows L* at Sites 1016 and 1021 but not at Site 1010. The color variables show the long-term, high-amplitude variation that correlates with the trends in carbonate content. Overprinted on this are Milankovitch-scale cyclicities that have much lower amplitude. In these sections, carbonate appears to be the dominant control on color composition. For Sites 1010 and 1021, with high BSi deep in the section and low values throughout the younger parts, a correlation between BSi and color is absent. At Site 1016, with lithologies consisting of diatoms and calcareous nannofossils mixed in variable proportions with each other and with clay, BSi content has a negative correlation with L* (i.e., BSi-rich intervals are darker than average). In carbonate-free sediments, high silica content usually corresponds to lighter than average sediments. Presumably, at Site 1016, lightness is more strongly influenced by carbonate in the three-component system of carbonate, clay, and BSi.

Figures 5 and 6 show the color record for the past 5 Ma in all sections for which an age interpolation was calculated. The northern shallow- and intermediate-water depth sites have generally subtle variation in composition, with low carbonate content and variable amounts of biogenic silica. In the color variables, this is reflected in low-amplitude time series and generally weak correlations with compositional data. Geochemical data will be collected at finer resolution in specific intervals to unravel what controls the subtle color variations in these sections. Still, even though the trends are low amplitude, the data show the presence of variation at the scale of orbital cycles. For example, L* in Sites 1018 and 1020 show the presence of cycles at the scale of 100 ka.

The highest amplitude high-frequency signal is found in the southern shallow- and intermediate-water depth section. Sites 1011 to 1014 have pronounced variation in TOC and carbonate content, which produces clear cycles in L* and b*. Overall, carbonate-rich sediments are lighter and more yellow, whereas organic-rich sediments are darker and more gray. Sites 1013 and 1014, which have the highest TOC content on average of all sites, are the only two sites that show a relatively high-amplitude signal in a*, with values periodically reaching moderately high positive values and with a positive correlation with TOC (i.e., organic-rich sediments contain a red component).

The color data presented here are one of the data sets that can be used for high-resolution correlation of sites with each other as well as fine tuning of the age-depth scale. At the resolution used for this study (1 cm), the color time series extracted from digital images are comparable with data that can be obtained with the Minolta spectrophotometer that is now part of the standard shipboard analytical tools, but was not yet used during Leg 167. The Oregon State University spectral reflectometer has similar spatial resolution, but can measure color in a wide range of wavelengths, which can be translated into a

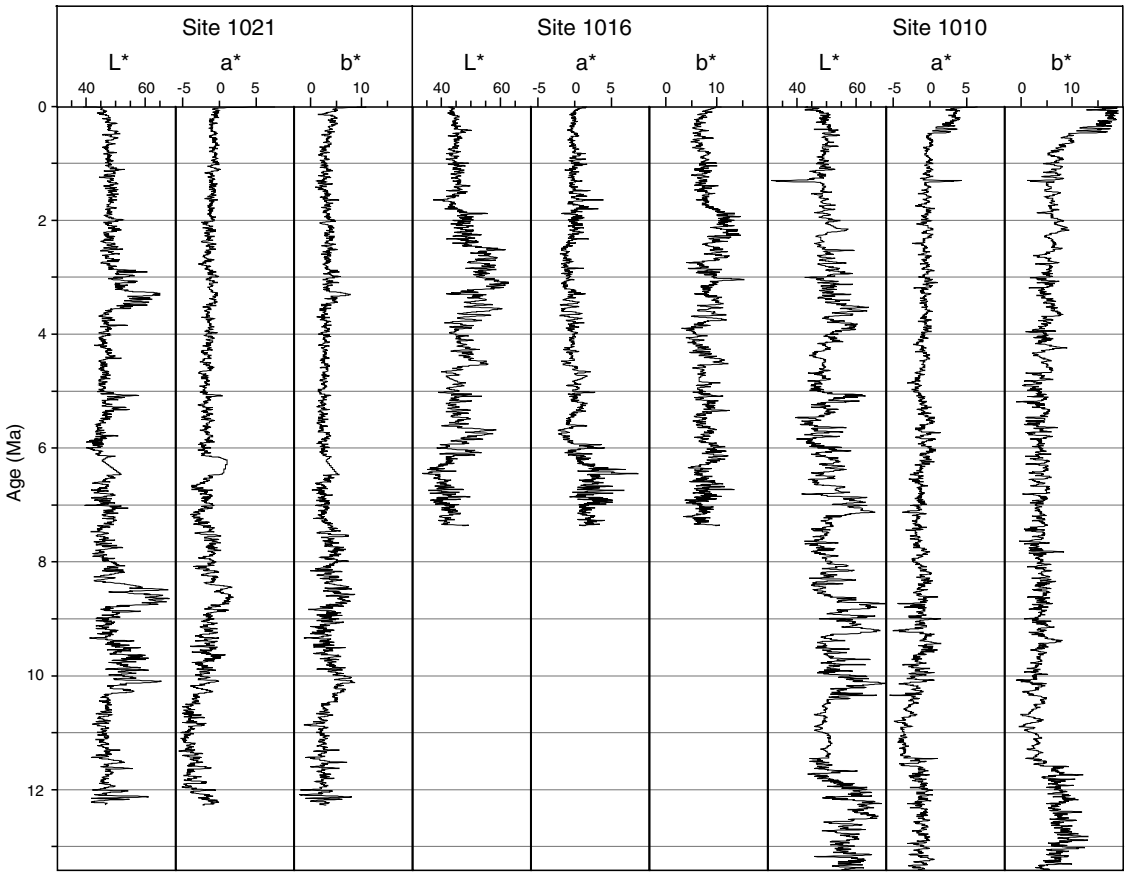

Figure 4. Color records against age in the deep-water sites. Average values were calculated over all data points in a 2-ka slice, and the resulting time series was smoothed with a 5-pt. unweighted running average.

good proxy for chemical sediment composition (Mix et al., 1995). In contrast, the video system as well as the Minolta system measure light only in three broad bands (red, green, and blue for the video system). Choice of method is mostly dependent on the actual application. Video images or still camera images can provide a real resolution of up to ~100 measurements per centimeter of sediment (or 0.1 mm), which allows registration of very fine-scale color variation, for example in laminated sediments (Merrill and Beck, 1995; Schaaf and Thurow, 1995, 1998). Methods presented here illustrate that after refinement of the light correction procedure, digital images can deliver good quality calibrated color data also at lower resolutions. A prerequisite is that the core surface is scraped carefully with a tool without sharp edges (e.g., a dough scraper) to remove scratches and other surface irregularities that would produce shadows or reflections causing artifacts in the image data.

REFERENCES

Billmeyer, F.W., Jr., and Saltzman, M., 1981. *Principles of Color Technology:* New York (Wiley).

Lyle, M., Koizumi, I., Richter, C., et al., 1997. *Proc. ODP, Init. Repts.,* 167: College Station, TX (Ocean Drilling Program).

Merrill, R.B., and Beck, J.W., 1995. The ODP color digital imaging system: color logs of Quaternary sediments from the Santa Barbara Basin, Site 893. *In* Kennett, J.P., Baldauf, J.G., and Lyle, M. (Eds.), *Proc. ODP, Sci. Results,* 146 (Pt. 2): College Station, TX (Ocean Drilling Program), 45–59.

Mix, A.C., Harris, S.E., and Janecek, T.R., 1995. Estimating lithology from nonintrusive reflectance spectra: Leg 138. *In* Pisias, N.G., Mayer, L.A., Janecek, T.R., Palmer-Julson, A., and van Andel, T.H. (Eds.), *Proc. ODP, Sci. Results,* 138: College Station, TX (Ocean Drilling Program), 413–427.

Rogers, D.F., 1985. *Procedural Elements for Computer Graphics:* New York (McGraw-Hill).

Schaaf, M., and Thurow, J., 1995. Late Pleistocene–Holocene climatic cycles recorded in Santa Barbara Basin sediments: interpretation of color density logs from Site 893. *In* Kennett, J.P., Baldauf, J.G., and Lyle, M. (Eds.), *Proc. ODP, Sci. Results,* 146 (Pt. 2): College Station, TX (Ocean Drilling Program), 31–44.

————, 1998. Two 30000 year high-resolution greyvalues time series from the Santa Barbara basin and the Guaymas Basin. *In* Cramp, A., MacLeod, C.J., Lee, S.V., and Jones, E.J.W. (Eds.), *Geological Evolution of Ocean Basins: Results from the Ocean Drilling Program.* Geol. Soc. Spec. Publ. London, 131:101–110.

Date of initial receipt: 28 October 1998
Date of acceptance: 19 April 1999
Ms 167SR-236

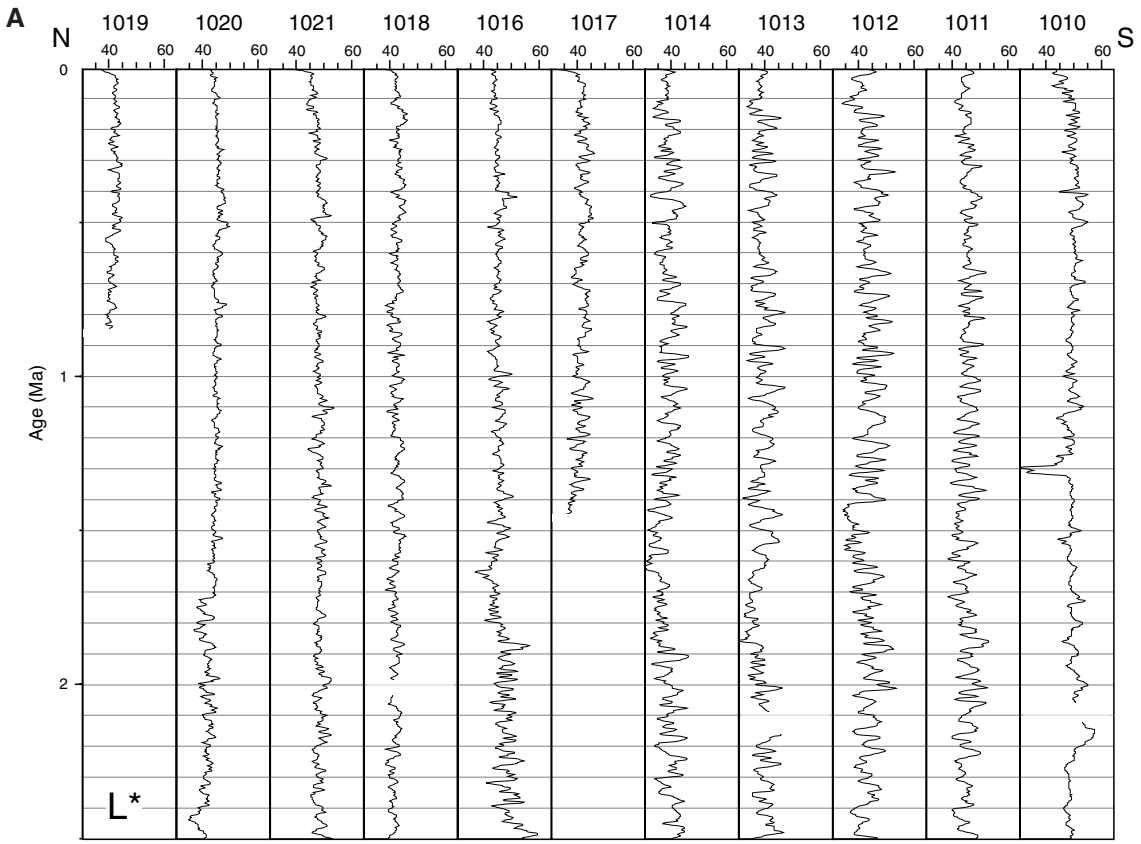

Figure 5. Color records against age for the last 2.5 m.y. in all sections arranged by latitude. **A.** L*. **B.** a*. **C.** b*. Average values were calculated over all data points in a 2-ka slice, and the resulting time series was smoothed with a 3-pt. unweighted running average. Note that horizontal scale in each color variable is the same for all sections, but that the intersect is different for Site 1014, to illustrate how amplitude of the signal varies between sites. (Continued on next page.)

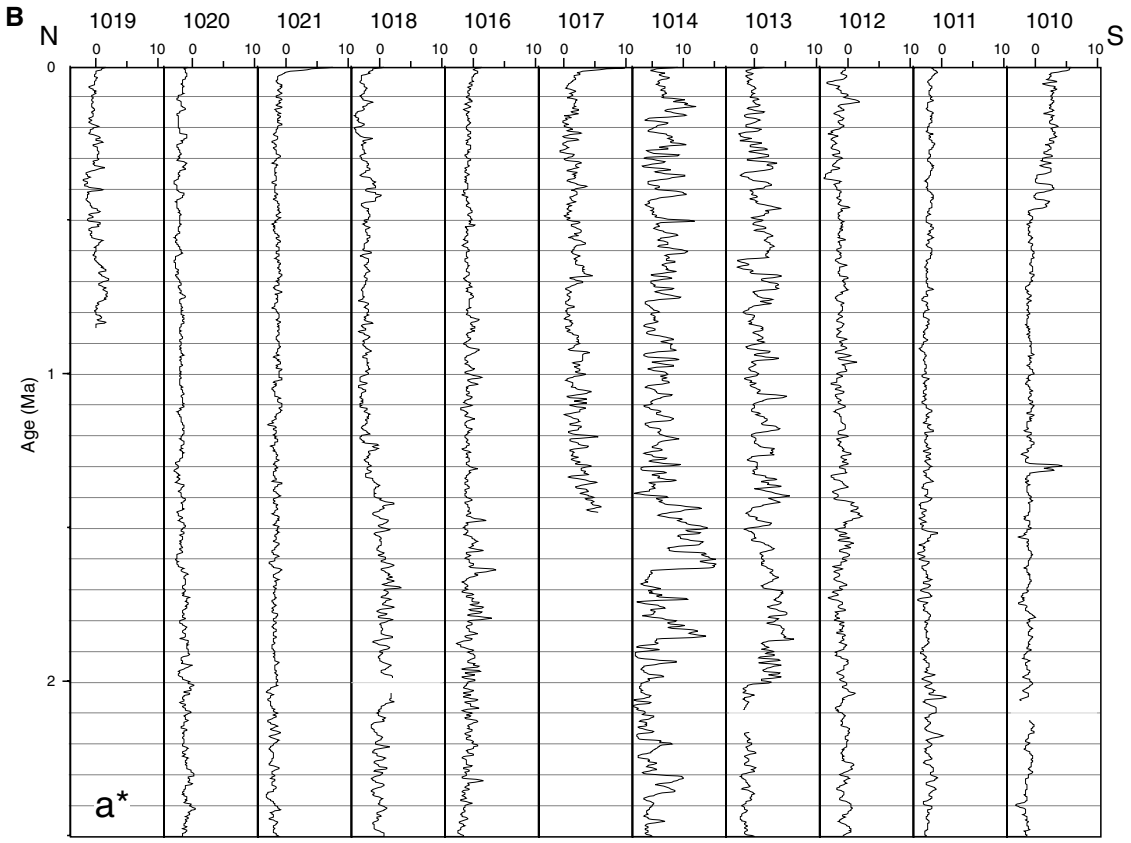

Figure 5 (continued).

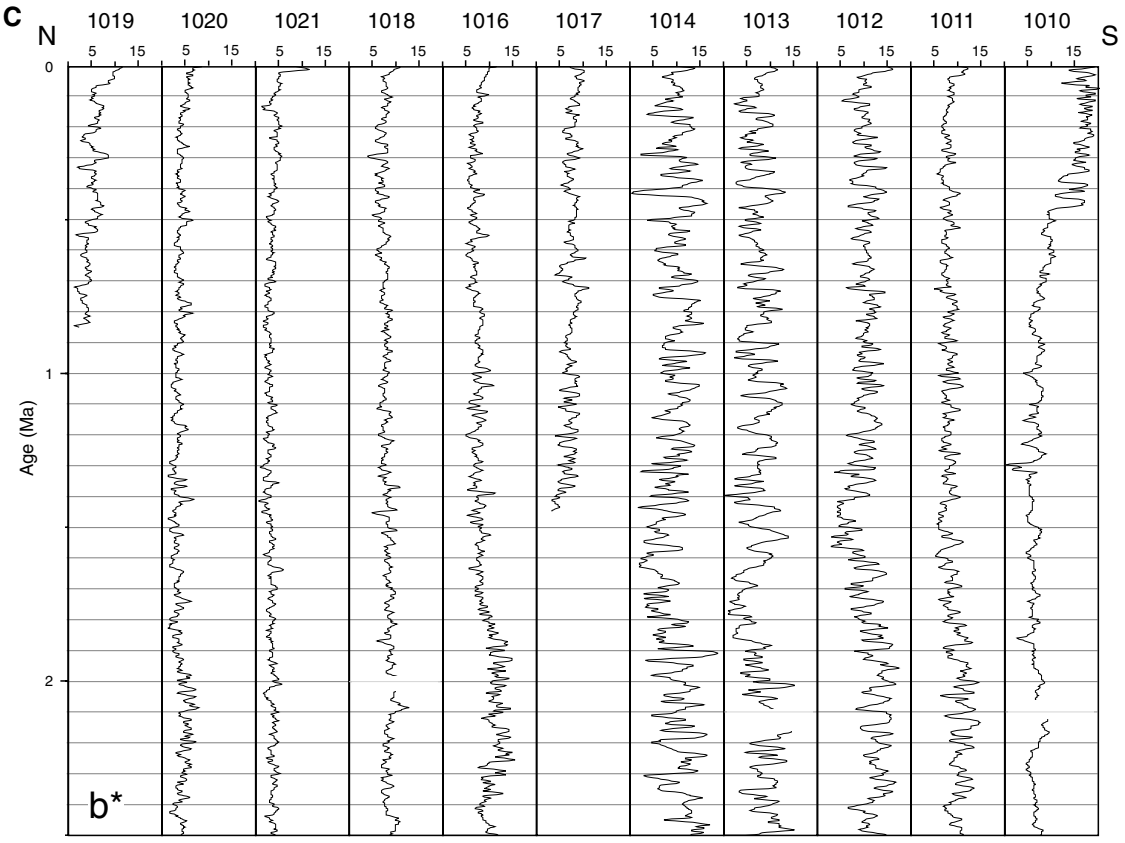

Figure 5 (continued).

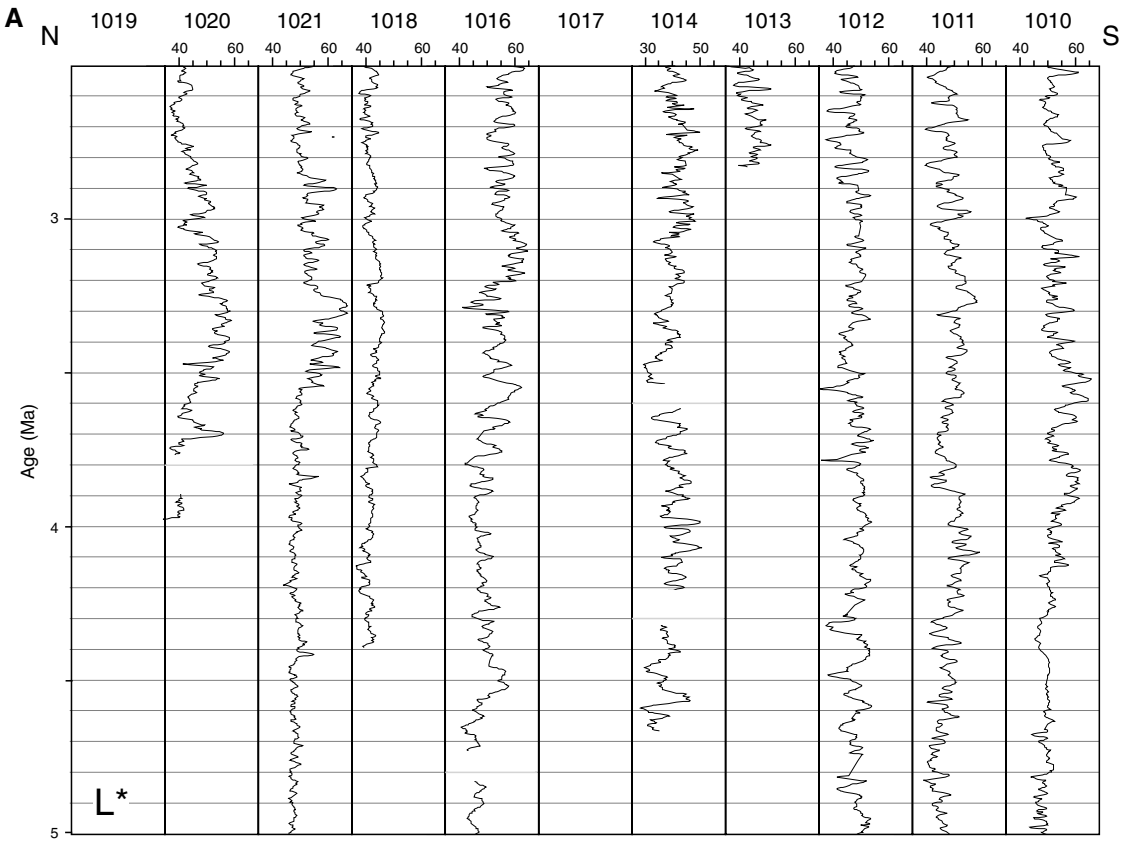

Figure 6. Color records against age for the 5- to 2.5-Ma interval in all sections arranged by latitude. **A.** L*. **B.** a*. **C.** b*. Note that boxes for Sites 1019 and 1017, which did not reach into sediments of this age, have been included for ease of comparison with Figure 5. For further explanation, see Figure 5. (Continued on next page.)

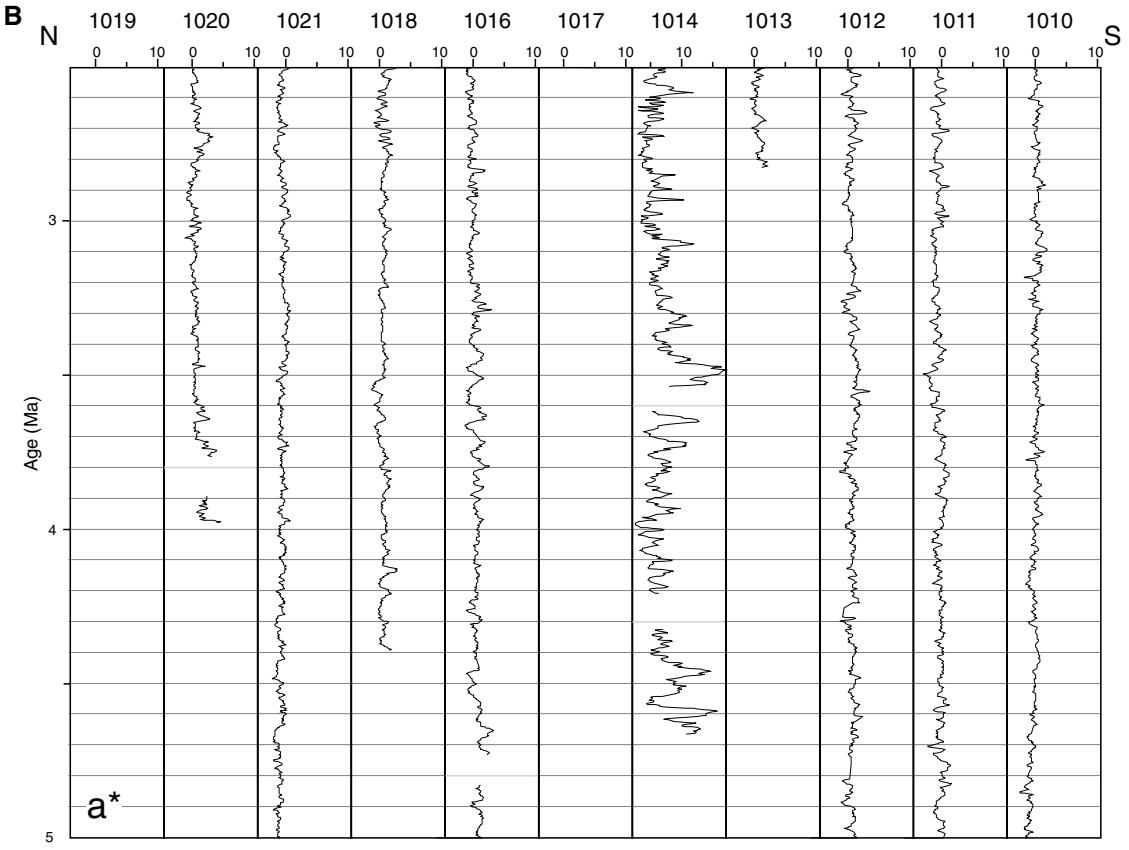

Figure 6 (continued).

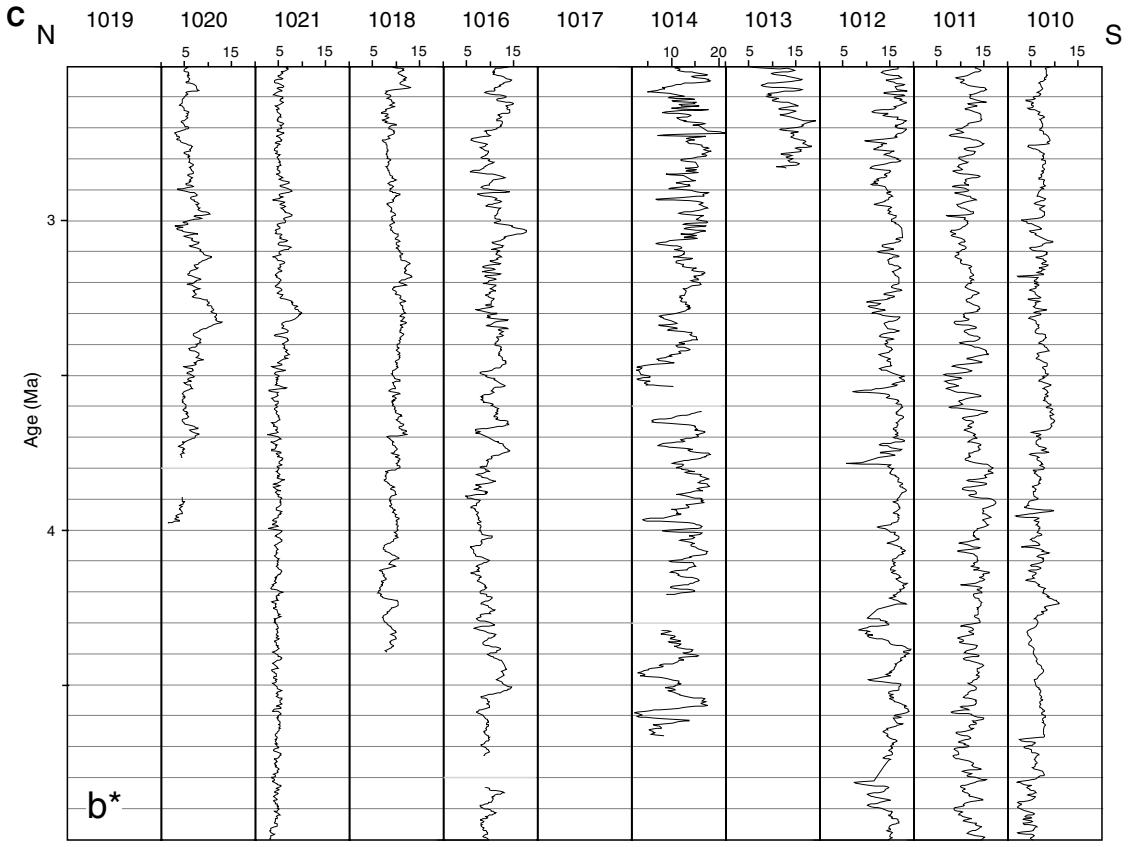

Figure 6 (continued).

Table 1. Correlation coefficients of color variables with each other and with shipboard measurements of carbonate and organic carbon content and of semiquantitative estimates of clay and biogenic silica content in smear slides.

Site	Color	a*	b*	$CaCO_3$	C_{org}	Clay	BSi
1010	L*	–0.22	0.09	**0.83**	**–**0.41	**–0.54**	–0.09
	a*		**0.56**	**–**0.04	0.26	0.22	–0.19
	b*			0.00	0.33	–0.37	0.31
1011	L*	–0.14	0.43	**0.73**	**–0.65**	**–**0.29	–0.21
	a*		0.36	0.18	**0.52**	0.08	0.03
	b*			**0.66**	**–**0.04	–0.30	0.16
1012	L*	–0.25	0.75	0.65	–0.80	**–0.75**	0.00
	a*		0.07	0.24	0.40	0.24	0.13
	b*			**0.79**	–0.42	**–0.56**	0.05
1013	L*	–0.70	0.95	**0.72**	**–0.80**	**–0.61**	**–**0.12
	a*		**–0.66**	–0.31	**0.66**	0.22	0.03
	b*			0.81	**–0.74**	**–0.58**	**–**0.17
1014	L*	**–0.86**	**0.94**	**0.62**	**–0.77**	**–0.65**	–0.20
	a*		**–0.77**	**–**0.11	**0.58**	0.44	0.24
	b*			**0.69**	**–0.69**	**–0.63**	**–**0.20
1016	L*	**–0.79**	0.38	**0.89**	**–**0.48	–0.27	**–0.54**
	a*		–0.12	**–0.58**	0.41	0.01	0.55
				0.53	–0.02	–0.47	–0.04
1017	L*	**–0.90**	**0.80**	0.24	**–0.72**	–0.06	–0.27
	a*		**–0.70**	**–**0.11	**0.71**	0.07	0.24
	b*			0.37	–0.54	–0.03	–0.18
1018	L*	–0.36	0.34	0.09	–0.37	0.33	**–0.60**
	a*		0.25	–0.28	**0.54**	–0.26	0.40
	b*			0.24	0.19	–0.32	0.24
1019	L*	**0.70**	0.34	**0.50**	**–**0.49	0.21	–0.18
	a*		–0.28	–0.21	0.27	–0.13	0.09
	b*			0.32	0.42	–0.16	0.38
1020	L*	–0.31	**0.61**	**0.75**	**–0.54**	**–0.61**	**–**0.22
	a*		0.02	–0.06	0.00	0.16	0.06
	b*			**0.54**	0.14	**–0.51**	0.13
1022	L*	**–0.54**	**0.58**	**0.88**	**–0.55**	0.02	–0.14
	a*		–0.37	0.10	0.33	–0.25	–0.02
	b*			**0.36**	0.12	–0.10	0.18

Notes: Biogenic silica (BSi) comprises the sum of all siliceous microfossils. Coefficients of 0.5 or higher are in boldface type to illustrate good correlation; given the number of data points, values of over 0.15 or 0.20 are significant for most sites.